Journal of Colloid and Interface Science 539 (2019) 332–341

Contents lists available at ScienceDirect

Journal of Colloid and Interface Science

journal homepage: www.elsevier.com/locate/jcis

Regular Article

Biomass-derived nitrogen-doped carbon quantum dots: highly selective fluorescent probe for detecting Fe^{3+} ions and tetracyclines

Houjuan Qi [a], Min Teng [a], Miao Liu [c], Shouxin Liu [a], Jian Li [a], Haipeng Yu [a], Chunbo Teng [c], Zhanhua Huang [a,*], Hu Liu [b,d], Qian Shao [e], Ahmad Umar [h], Tao Ding [f,*], Qiang Gao [g,i,*], Zhanhu Guo [b,*]

[a] College of Material Science and Engineering, Northeast Forestry University, Harbin 150040, China
[b] Integrated Composites Laboratory (ICL), Department of Chemical and Bimolecular Engineering, University of Tennessee, Knoxville, TN 37996, USA
[c] College of Life Science, Northeast Forestry University, Harbin 150040, China
[d] National Engineering Research Center for Advanced Polymer Processing Technology, Zhengzhou University, Zhengzhou 450002, China
[e] College of Chemical and Environmental Engineering, Shandong University of Science and Technology, Qingdao, Shandong 266590, China
[f] College of Chemistry and Chemical Engineering, Henan University, Kaifeng 475004, China
[g] Department of Heterogeneous Catalysis, Max Planck Institute for Chemical Energy Conversion, 45470 Mülheim an der Ruhr, Germany
[h] Department of Chemistry, Faculty of Sciences and Arts, Promising Centre for Sensors and Electronic Devices (PCSED), Najran University, P.O. Box 1988, Najran 11001, Saudi Arabia
[i] School of Chemical Engineering, Southwest Forestry University, Kunming 650224, PR China

GRAPHICAL ABSTRACT

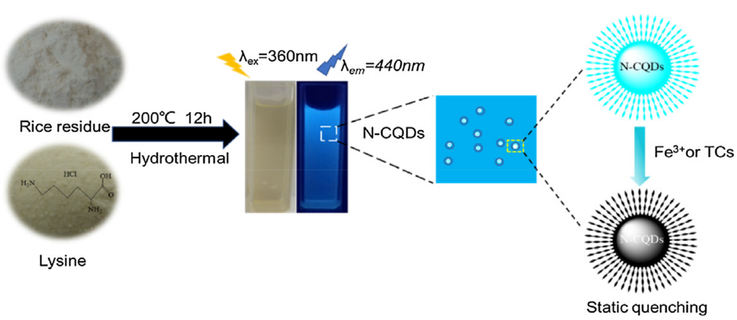

ARTICLE INFO

Article history:
Received 4 November 2018
Revised 5 December 2018
Accepted 12 December 2018
Available online 13 December 2018

Keywords:
N-CQDs
Label-free detection
Fe^{3+} and TCs detection
Fluorescent probe

ABSTRACT

Nitrogen-doped carbon quantum dots (N-*CQDs*) were successfully synthesized using rice residue and glycine as carbon and nitrogen sources by one-step hydrothermal method. High quantum yield (23.48%) originated from the effective combination of nitrogen with various functional groups (C═O, N—H, C—N, COOH and C—O—C). The N-CQDs showed a fluorescence with the wavelength varied from 420 to 500 nm and the maximum emission wavelength being at 440 nm. N-CQDs have been importantly applied as probe to detect Fe^{3+} and tetracycline (TCs) antibiotics with remarkable performance. Using the linear relationship between fluorescence intensity and Fe^{3+} concentration, the N-CQDs could be employed as a simple, efficient sensor for ultrasensitive Fe^{3+} detection ranging from 3.32 to 32.26 μM, with a limit of detection (LOD) of 0.7462 μM. The N-CQDs showed the applicability to detect TCs. The detection limits of tetracycline, terramycin and chlortetracycline were 0.2367, 0.3739 and 0.2791 μM, respectively. The results of TC by fluorescence method in real water samples were in good agreement with standard

* Corresponding authors at: College of Material Science and Engineering, Northeast Forestry University, Harbin 150040, China (Z.H. Huang); College of Chemistry and Chemical Engineering, Henan University, Kaifeng 475004, China (T. Ding); School of Chemical Engineering, Southwest Forestry University, Kunming 650224, PR China (Q. Gao); Integrated Composites Laboratory (ICL), Department of Chemical and Bimolecular Engineering, University of Tennessee, Knoxville, TN 37996, USA (Z.H. Guo).
E-mail addresses: huangzh1975@163.com (Z. Huang), dingtao@henu.edu.cn (T. Ding), Qiang.Gao@cec.mpg.de (Q. Gao), zguo10@utk.edu (Z. Guo).

https://doi.org/10.1016/j.jcis.2018.12.047

Ultraviolet–visible (UV–vis) method. The N-CQDs have various potential applications including sensitive and selective detection of Fe^{3+} and TCs, and cellular imaging with low cytotoxicity, good biocompatibility and high permeability.

1. Introduction

Carbon quantum dots (CQDs) have attracted remarkable attention as a novel and promising fluorescent carbon material thanks to their unique optical properties, good water solubility, high stability, low toxicity, excellent biocompatibility and low environmental impact [1]. CQDs have shown various applications including cellular imaging [2], fluorescent ink [3], photocatalysis [4,5], drug delivery [6], detection of ions (such as Hg^{2+} [7,8], Fe^{3+} [3,9], Zn^{2+} [8], Cu^{2+} [10,11], F^{-} [12], Eu^{3+} [12], and As^{3+} [13]), and detection of organics (including pesticides [14], methimazole [1], glutathione [15], nitro-compounds [16], α-glucosidase [17], chitosan [18], cholesterol [19] and picric acid [20]). In the past few years, there have been numerous reports of natural biomass being used as a carbon source for CQD synthesis as an alternative to chemical carbon sources. Natural biomasses include orange juice [21], hair [22], sugarcane bagasse pulp [23], walnut shells [24], petroleum coke [25], egg [26] and jinhua bergamot [27], etc. These carbon sources present to be cheap, green and sustainable. However, the quantum yield (QY) of natural biomass is low and has to be improved. The QY is a vital property of CQDs and dictates the possible applications. Heteroatom doping of CQDs not only improves the fluorescence efficiency, but also provides active sites in the CQDs to broaden their potential applications in the analysis and sensing. Due to the atomic size and chemical valence of nitrogen atoms, the nitrogen-doped CQDs (N-CQDs) are of great interests. For example, Madrakian et al. [28] proposed an isotretinoin detection system with a 0.03 μM limit of detection (LOD) using an N-CQD-based fluorescence sensor, which had been applied as a bio-probe for isotretinoin detection in pharmaceutical preparations and human serum samples. Niu et al. [29] used a controllable electrochemical/electroanalytical approach to generate aspartic acid (Asp) based NCQDs (Asp-N-CQDs), which exhibited the highest QY and were applied as probes for the Fe^{3+} detection in cells. The Asp-N-CQDs as nanosensor probes for the Fe^{3+} detection showed a low LOD of 0.5 μM.

Iron ions (Fe^{3+}) play a crucial role in the biological system and present in all tissues, especially in liver, spleen and lung. An imbalance of Fe^{3+} content regulation can cause diseases such as anemia, Alzheimer's disease, Parkinson's disease, intelligence decline, hemochromatosis, diabetes and cancer [30,31]. Therefore, the detection of Fe^{3+} holds a great promise for the early diagnosis of these diseases. The typical Fe^{3+} detection techniques include plasma-optical emission spectrometry [32] and colorimetry [33]. However, these methods are complex and expensive, and the detection is limited by the precision of the instruments. Optical method shows a more cost-effective way due to its relatively low cost compared with instrumental methods. Among these, fluorescence spectrometer is a novel method with good selectivity, high sensitivity and wide linear range for rapid and simple testing of metal ions. The fluorescence sensor can be used not only in the detection of some heavy metal ions but also in the study of protein and other researches.

Tetracyclines (TCs) are widely used as antibiotics in veterinary and human medicine and tend to accumulate in food products because of their excessive abuse as growth promoters, and pose serious risk to human health [34]. The damages arising from the abuse of TCs include yellowing of teeth, liver damage and allergic reactions. The methods used for detecting TCs are capillary electrophoresis, colorimetry [35], immunoassays and high-performance liquid chromatography [36,37]. However, most of these methods involve sophisticated instrumentation, which limit their LOD, sensitivity and selectivity, and introduce high instrument maintenance costs. Fluorescence technologies are considered as a simple, rapid, economical, sensitive and selective method of TCs detection, especially when a larger number of samples must be processed. N-CQD application as a fluorescent probe, observed using a fluorescence microscope, can provide information on cellular pools of metal ions and TCs and their responses to changes in biological stimuli and environment. In the processing of rice, a lot of produced rice residue are used as fodder and cannot reflect its real value. Rice residue contains rich protein and carbohydrates that can serve as carbon and nitrogen sources for CQDs. The application from rice-residue derived CQDs to detect both Fe^{3+} and TCs has not been reported yet.

In this work, a facile method for synthesizing highly fluorescent N-CQDs via a one-step thermal treatment of rice residue was reported. Highly selective and sensitive detections of Fe^{3+} and TCs were investigated by fluorescent quenching. N-CQDs served as a crucial fluorescent probe for the detection of Fe^{3+} and TCs, and for the cellular imaging. The practical application of Fe^{3+} and TCs in tap water and river water was studied by fluorescent method, atomic absorption spectroscopy (AAS) and UV–vis as comparisons.

2. Materials and methods

2.1. Materials

Rice residue was collected by a local factory (Harbin, China). Fetal bovine serum (FBS) was purchased from BI (Israel). Other cell culture reagents were purchased from HYCLONE Co. (USA). Chemical reagents were purchased from Tianjin Kemiou Chemical Reagent Co., Ltd. (Tianjin, China). All reagents were analytical grade and used without further purification.

2.2. Characterization

X-ray photoelectron spectroscopy (XPS) of N-CQDs was carried out using K-Alpha with Al X-rays at 140 W (THERMO, USA). Fourier-transform infrared spectroscopy (FT-IR) was performed using an iS 10 FT-IR spectrometer (Thermo Nicolet Co., MA, USA). Ultraviolet–visible (UV–vis) absorption spectroscopy was carried out using a TU-1950 spectrophotometer (Beijing Purkinje General Instrument Co., Ltd. China). Transmission electron microscopy (TEM) images and high resolution TEM (HRTEM) images were acquired using a JEM-2100 transmission electron microscope (LJEMOC, Japan). Fluorescence was measured using a LS-55 fluorescence spectrophotometer (Perkin-Elmer, USA). The fluorescence microscope used was a DeltaVision™ Elite Cell Imaging System (GE, USA). An ultraviolet fluorescence analyzer was used to observe fluorescence phenomena (Shanghai Jingke Industrial Co., Ltd. China). The details of the instruments are described in Supplementary information (S1).

2.3. Synthesis of N-CQDs

The N-CQDs were prepared using a previously reported hydrothermal method [3]. Briefly, rice residue and lysine were mixed in deionized water at a mass ratio of 4:1. After dispersion by stirring (20 min), the mixture was transferred to a 50 mL Teflon-lined stainless-steel autoclave and heated at 200 °C for 12 h in an air oven. After cooling down to room temperature and centrifugation to remove large particles and impurities, the product was purified using a 0.22 μm filter membrane and stored at 4 °C for future use.

2.4. Fluorescence quantum yield (QY)

The QY of N-CQDs was tested as previously reported [38]. The QY was calculated according to Eq. (1) using quininesulfate (QY = 54% in 0.1 M H_2SO_4 at 350 nm) as the standard sample:

$$QY(\%) = QY_R \frac{I_S A_R (n_S)^2}{I_R A_S (n_R)^2} \tag{1}$$

where I is the fluorescent emission intensity, n is the refractive index of the solvent, and A is the absorbance. The subscripts R and S denote known fluorescent standard samples and experimental samples, respectively.

2.5. N-CQD Detection of ions

The detection of Fe^{3+} was conducted in a phosphate buffer solution (pH = 4) with a fluorescence excitation wavelength of 360 nm at room temperature. The concentrations of N-CQDs were 200 μg mL^{-1} for selectivity study and 50 μg mL^{-1} for sensibility study. The sensibility study was carried out using fluorescence spectroscopy to measure different concentrations of Fe^{3+} (0–250 μM). The selectivity study was performed with various ions (Ni^{2+}, Ag^+, Cd^{2+}, La^{3+}, Pb^{2+}, Co^{2+}, Ce^{3+}, K^+, Na^+, Ca^{2+}, Y^{3+}, Zr^{4+}, Al^{3+}, Mg^{2+}, Cu^{2+}, Hg^{2+}, Fe^{3+}, Fe^{2+}, PO_4^{3-}, Cl^-, SO_4^{2-}, CO_3^{2-} and NO_3^-) with a concentration of 62.5 μM. Following 2 min reaction period at room temperature, the fluorescence emission response was recorded under consistent conditions.

2.6. N-CQD Detection of tetracycline antibiotics

3 mL N-CQDs (200 μg mL^{-1}, pH = 4) and 200 μL 0.1 mM organics (Lysine, BSA, EDTA, Tetracycline (TC), Chlortetracycline (CTc), Erythromycin, Cysteine, Terramycin (OTc), Glycine, Glucose and Vitamin C) were mixed and transferred to a cuvette. The selectivity was demonstrated against 11 different organics. The sensibility study was carried out using fluorescence spectroscopy and different concentrations of TC, CTc and OTc (0–250 μM) with a fixed concentration (50 μM) of N-CQDs. After reaction at room temperature for 10 min, the measurements were recorded under consistent conditions at a fluorescence excitation wavelength of 360 nm.

2.7. Cytotoxicity assay

Cell culture. Human hepatoma HepG2 liver cells were maintained in RPMI 1640 medium supplemented with 10% fetal bovine serum and 100 mg mL^{-1} penicillin G-streptomycin, at 37 °C in 5% CO_2 humidified environment. At confluence, the cells were washed with phosphate buffered saline and treated with trypsin/EDTA to release into suspension. Finally, the cells were washed and re-suspended with fresh medium to achieve the desired cell density.

Cellular toxicity test. The cellular toxicity test was carried out according to a previously reported method [39]. The cytotoxicity of as-prepared CQDs was investigated using the CCK-8 assay with HepG2 cells. The HepG2 cells were seeded in a 96-well plate (100 μL per well). The CQD and N-CQD solutions with different concentrations (0, 10, 25, 50, 100, 200 μg mL^{-1}) were then added in triplicate and the cells were incubated for 24 h at 37 °C in a humidified CO_2 environment. Each cell was incubated with 10 μL CCK-8 solution for 2 h away from light, before measuring the absorbance at 450 nm with a microplate reader (Sunrise™, Tecan, Männedorf, Switzerland). The cell survival rate was calculated by eqn (2):

$$\text{Cell survival rate}(\%) = \frac{A_{withCQDs} - A_{blank}}{A_{withoutCQDs} - A_{blank}} \times 100\% \tag{2}$$

where $A_{with\ CQDs}$ is the absorbance of the solution in the well with HepG2 cells, CCK-8 solution and CQDs, A_{blank} is the absorbance of the solution in the well with culture medium, and CCK-8 solution, and $A_{without\ CQDs}$ is the absorbance of the solution in the well with HepG2 cells and CCK-8 solution.

Fluorescence microscopy cell imaging. The bio-imaging test for the as-prepared N-CQDs was performed using HepG2 cells. Staining was achieved by cultivating the cells in the presence or absence of the respective N-CQDs in a humidified chamber at 37 °C for 24 h. The cells were washed and fixed with 1 mL 4% (w/v) paraformaldehyde for 0.5 h at room temperature. The fluorescence of the stained cells was observed and imaged using an appropriate filter (blue, green and red) on a fluorescence microscope (DeltaVision™ Elite Cell Imaging System, GE, USA).

2.8. Determination of real samples

River water and Tap water were collected from Songhua River (Harbin, China) and Mao Er Mountain natural mineral water (Harbin, China). All the raw samples were pretreatment, the samples were centrifuged (14800 g, 20 min) and filtered through a 0.22 μm membrane to remove the suspended particles. The Fe^{3+} and TC concentrations in real water samples were evaluated by Fluorescence spectroscopy and UV–vis absorption spectroscopy (UV–vis).

3. Results and discussion

3.1. Structural characterization of the N-CQDs

The FT-IR spectra have been first employed to characterize the N-CQDs (Fig. 1a). The characteristic peaks at 3200 and 3441 cm^{-1} represent the stretching vibrations of N—H and O—H. Moreover, the small peaks at 2921 and 2863 cm^{-1} are the stretching vibration band of -CH_2 groups [25]. The peaks at 1641 cm^{-1} and 1581 cm^{-1} are consistent with the bending vibrations of the CO-NH group [28]. The characteristic peaks at 1448, 1767, 1136 and 1033 cm^{-1} are attributed to C—N, C═O, C—O—C and C—O, respectively [40]. XPS analysis shows the surface composition and chemical environment of the N-CQDs. The XPS survey spectrum of N-CQDs shows the peaks at 284.51, 406.99 and 532.44 eV, corresponding to C1s, N1s and O1s electrons, respectively (Fig. 1b). The high-resolution spectrum of the C1s signal shows five peaks at 284.59, 284.9, 285.6, 286.4and 287.3 eV, representing the C—C /C═C, C—H, C—O, C—O—C and C═O groups, respectively [3,8]. In the high-resolution N1s spectrum (Fig. 1d), the three peaks at 399, 399.7 and 400.7 eV could be assigned to the C═N, N—H and C—N groups, respectively [8,41]. The O1s spectrum (Fig. 1e) shows three fitted peaks at 530.5, 531.4 and 532.6 eV, attributing to the HO-C═O, C═O and C-OH/ C—O—C groups, respectively [3,8,42,43]. The XPS analysis results of the C1s, N1s and O1s spectra are consistent with the FT-IR analysis.

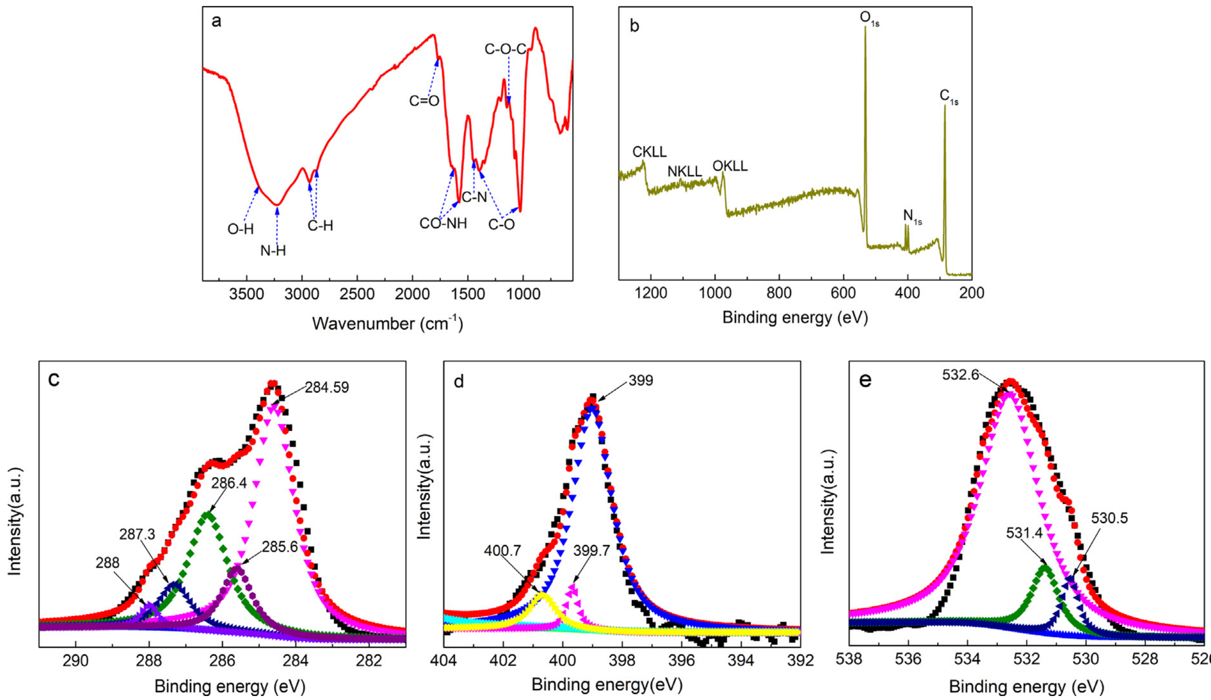

Fig. 1. (a) FT-IR spectra of the N-CQDs; (b) XPS survey spectrum; (c) High-resolution C1s peaks and fitting curves; (d) High-resolution N1s peaks and fitting curves; (e) High-resolution O1s peaks and fitting curves.

3.2. TEM analysis

The morphology and microstructure of N-CQDs dispersed in water were characterized by HRTEM (Fig. 2a and 2b). The HRTEM images indicate that N-CQDs were spherical, well dispersed and uniform with an average diameter of 2.70 nm. The HRTEM image shows that most particles are amorphous carbon without obvious lattice fringes [8,44].

3.3. Optical properties of N-CQDs

Optical properties of N-CQDs were studied using UV–vis and fluorescence spectroscopies. The N-CQDs showed bright blue fluorescence under 365 nm UV irradiation (Fig. S1, supporting information). The strong blue fluorescence is visible with the naked eye. However, the solution showed no perceptible PL without UV irradiation and remained transparent, pale yellow and transparent under daylight. This behavior suggested that the surface groups and size of the N-CQDs were important factors in their blue PL emission [45]. The UV–vis spectra of N-CQDs showed the peaks at 340 and 280 nm (Fig. S1). The peak at 280 nm is ascribable to the π-π* transition for the C═C bond, in which the orbital was sp^2 hybridized clusters [22]. The absorbance at 340 nm corresponds to the n-π* transition of the C═O and N─H groups. The spectra show that the intensity and peak positions of the FL emissions depend on the excitation wavelength (Fig. 2c). The fluorescence study was carried out at different excitation wavelengths. The emission wavelength was shown to increase with increasing the excitation wavelength. As the excitation wavelengths varied from 280 to 400 nm, the maximum intensity of the emission peak decreased, and the peaks shifted to longer wavelengths (red shift), owing to the difference in particle size of the N-CQDs and in the distribution of emissive trap sites. The optical excitation (λ_{ex} = 360 nm) and emission wavelengths (λ_{em} = 440 nm) of N-CQDs were obtained from the fluorescence emission and excitation spectra, respectively.

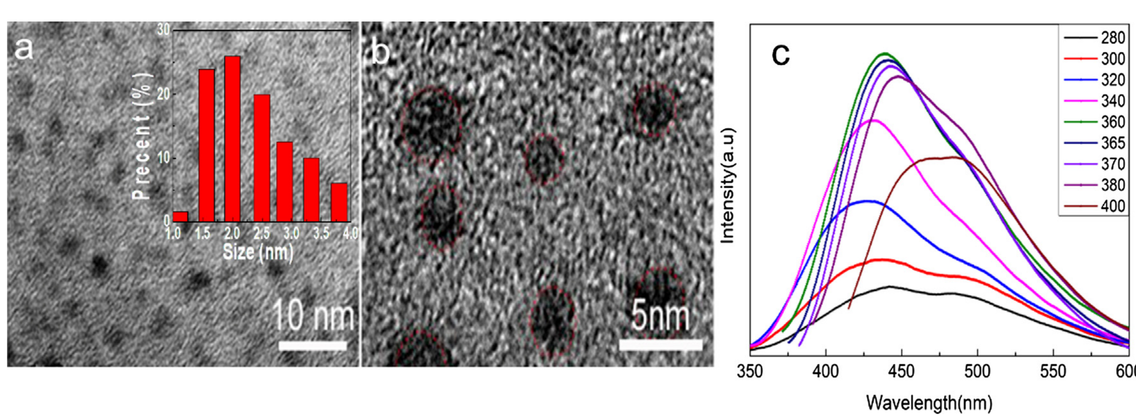

Fig. 2. (a-b) HRTEM images of N-CQDs with different magnification (Insert in (a) was size distribution (statistics: 100 measurements from TEM image) of N-CQDs). The fluorescence properties of N-CQDs solutions, (c) Excitation dependent fluorescence emission spectra of N-CQDs.

3.4. Detection of Fe^{3+}

Selectivity and sensitivity studies. Selectivity plays a critical role in establishing the sensing properties of QD detection methods. The fluorescence quenching performance has been studied in the presence of 17 cations and 5 anions in 0.1 M solutions using an excitation wavelength of 360 nm. Fig. 3a shows the images of N-CQDs in blank solution and with different metal ions including, Ni^{2+}, Ag^{+}, Fe^{2+}, Cd^{2+}, La^{3+}, Pb^{2+}, Co^{2+}, Ce^{3+}, K^{+}, Na^{+}, Ca^{2+}, Y^{3+}, Zr^{4+}, Al^{3+}, Mg^{2+}, Cu^{2+}, Hg^{2+}, PO_4^{3-}, Cl^{-}, SO_4^{2-}, CO_3^{2-} and NO_3^{-} under UV irradiation (λ = 365 nm). The corresponding fluorescence emission spectra are shown in Fig. S2. The Fe^{3+} ion demonstrated the marked fluorescence quenching compared with other ions tested. The fluorescence of N-CQDs is quenched by Fe^{3+} ions because of the special coordination between Fe^{3+} ions and phenolic hydroxyl groups on the surface of N-CQDs. The fluorescence quenching of N-CQDs in Fe^{3+} ion solution may contribute to nonradiative electron-transfer, in which partial electrons were transferred to the d-like states of Fe^{3+} ions [45]. The fluorescence quenching was also fast, occurring ~ 1 min after adding the Fe^{3+} solution to the cuvette, and remained constant over a period of 20 min (Fig. 3d). The rapid fluorescence quenching might be due to the efficient energy transfer between Fe^{3+} and the groups on the surface of the N-CQDs [45]. It becomes obvious that N-CQDs are applicable as a fluorescent sensor for sensitive and selective detection of Fe^{3+} ions.

The fluorescence could be quenched gradually with increasing the concentration of Fe^{3+} (Fig. 3b). Accordingly, I/I_0 decreased with increasing the concentration of Fe^{3+} ions and displayed a good linear relationship in the range of 3.32–32.26 μM with a linear correlation coefficient (R^2) of 0.987 (Fig. 3c). The LOD of 0.7462 μM was established for this system according to Eq. (3) [3]:

$$LOD = \frac{3\delta}{s} \tag{3}$$

where δ is the standard deviation of the signals and s is the slope of straight line. Furthermore, the analytical performances such as the sensitivity and linear range are comparable or even better than those reported previously (Table S3), showing their promising applications in biomedical and environmental systems.

Possible Quenching Mechanism. Fluorescence quenching is caused by the interaction between fluorescent molecules and inhibitory molecules and is usually divided into static quenching and dynamic quenching. The fluorescence was quenched dramatically with increasing the Fe^{3+} concentration. The fluorescence quenching was fitted using the Stern-Volmer equation by Eq. (4) [46,47]:

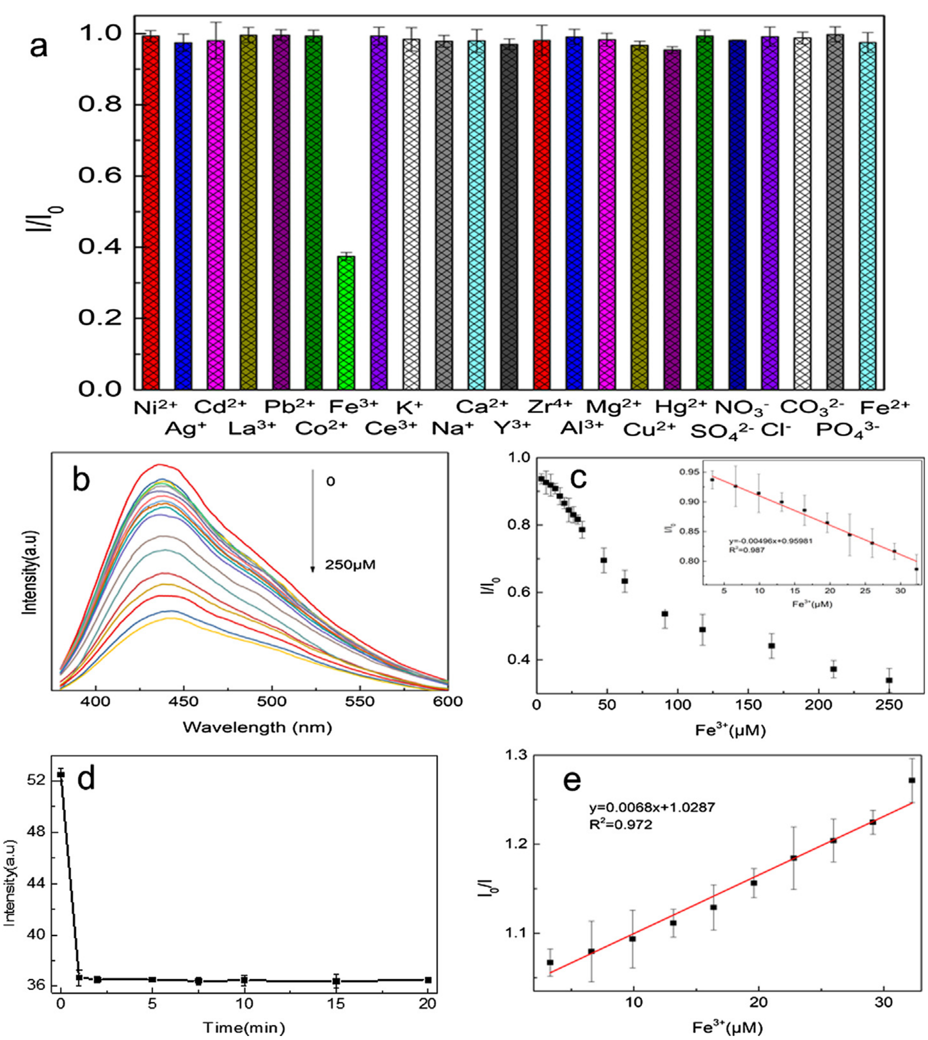

Fig. 3. (a) Influence of different ions on the fluorescence of N-CQDs; (b) Fluorescence intensity dependence on concentration of Fe^{3+}; (c) Fluorescence intensity ratio (I/I_0) of N-CQDs with various concentrations of Fe^{3+}(Insert in (c) was linear relationship between I/I_0 and the concentration of Fe^{3+} in the range of 3.32–32.26 μM); (d) Time-dependent fluorescence signal of N-CQDs based on the quenching time; (e) Linear relationship of I/I_0 with concentration of Fe^{3+} in the range of 3.32–32.26 μM. (The number of repeat experiments was five times).

$$\frac{I_0}{I} = 1 + K_{sv}[Q](R^2 = 0.9722) \quad (4)$$

where I_0 and I are the fluorescence intensities at emission wavelength 440 nm in the absence and presence of Fe^{3+}, respectively. [Q] is the concentration of Fe^{3+}, and K_{sv} is the Stern-Volmer quenching constant. The K_{sv} was $6.8 \times 10^3\ M^{-1}$ ranging from 3.32 to 32.26 μM for a linear regression equation (Fig. 3e). According to the double molecular quenching constant (K_q) $K_q\tau_0 = K_{sv}$, τ_0 was already known, thus Kq was $1.8256 \times 10^{12}\ L\ mol^{-1}\ s^{-1}$, which was much larger than the reported maximum collision quenching constant ($2.0 \times 10^{10}\ L\ mol^{-1}\ s^{-1}$) for the quenching fluorescence molecules. The observed quenching could be static quenching [48], and was caused by the formation of non-fluorescent complexes when the quenching agent was combined with the fluorescent material molecules in the ground state. The fluorescence lifetime study is a useful method for distinguishing between dynamic quenching and static quenching. Fluorescence lifetime was tested for the N-CQDs in the absence and presence of Fe^{3+} (Fig. S3). By adding Fe^{3+}, the fluorescence lifetime of the N-CQDs exhibited almost no change, extending from 3.7248 to 3.9119 ns (Table S1). The τ/τ_0 value tended to 1, indicating that the fluorescence quenching caused by Fe^{3+} addition was probably static quenching.

3.5. Tetracycline analog sensitivity and selectivity

Selectivity and sensitivity studies. The selectivity study was carried out using different organic molecules and an excitation wavelength of 360 nm. As shown in Fig. 4a, tetracycline analogs such as TC, CTc, and OTc were used. Fig. 4b presents fluorescence images of N-CQDs in blank samples and with different organic molecules under UV irradiation (λ = 365 nm). By adding TCs, the fluorescence significantly decreased. The fluorescence quenching is visible with the naked eye. The chemical structures of TC, CTc and OTc are shown in Fig. S4. Because of their structural similarity to TC, both OTc and CTc could also access the recognition sites and quench the fluorescence of the sensor. The fluorescence intensity of N-CQDs (50 μg mL^{-1}) decreased when the concentration of TC (0–250 μM) increased (Fig. 4d). Calibration plots were generated under the established optimum experimental conditions. Accordingly, I/I_0 decreased with increasing the concentration of TC and displayed a good linear relationship in the range of 3.32–32.26 μM with a linear correlation coefficient (R^2) of 0.983 (Fig. 4d). In addition, OTc and CTc showed good fluorescence responsiveness. The outcomes for OTc and CTc held good linear correlation of 0.9950 and 0.9869, respectively (Fig. S5). According to Eq. (2), the detection limits of OTc, CTc and TC were 0.3739, 0.2791 and 0.2367 μM, respectively. N-CQDs have shown to be a selective and eco-friendly sensor for detecting tetracycline analogs, indicating great promise for applications in environmental monitoring.

3.6. In vitro cytotoxicity and cell imaging of N-CQDs in HepG2 cells

Cell cytotoxicity. To evaluate the cytotoxicity of N-CQDs and establish their potential as bio-imaging materials, CCK-8 assays

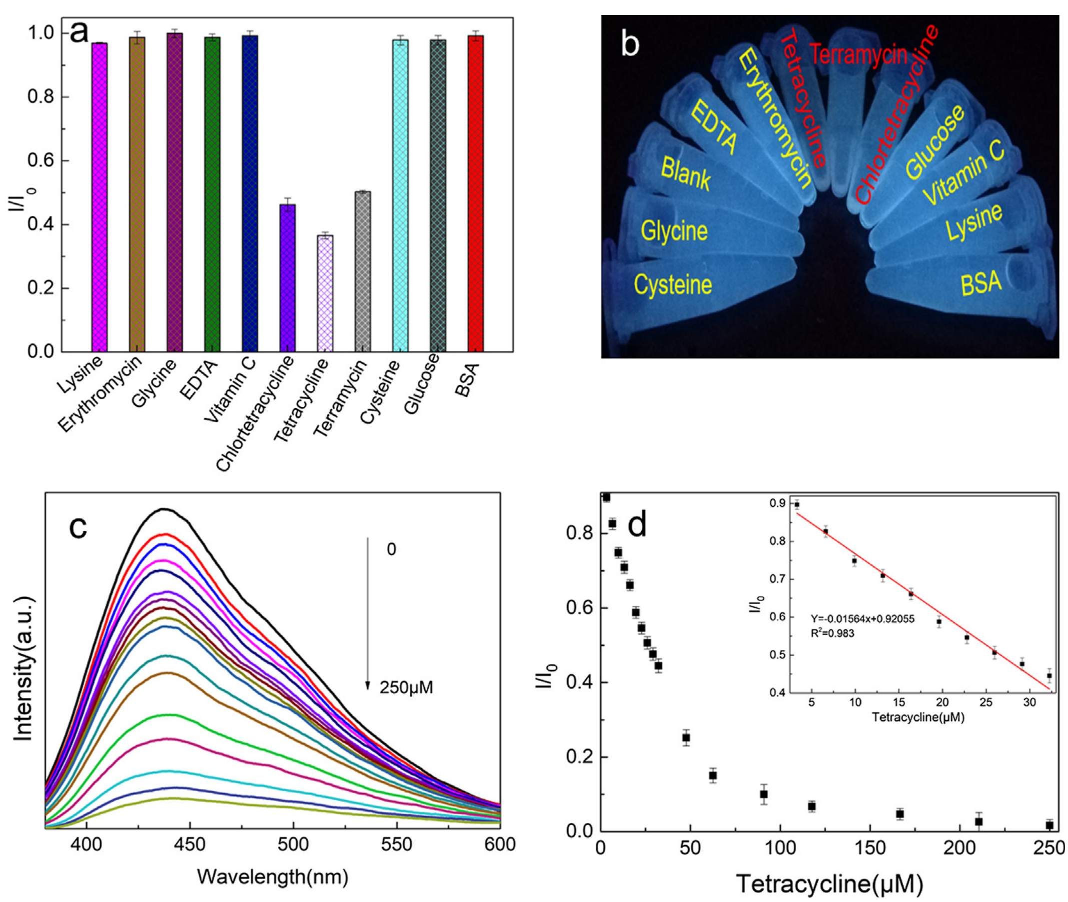

Fig. 4. (a) PL intensity of N-CQDs in aqueous solution when different organic molecules were introduced; (b) Fluorescence images of N-CQD solutions with various organic molecules under UV irradiation (λ = 365 nm); (c) Fluorescence intensity dependence on conentration of TC; (d) Fluorescence intensity ratios (I/I_0) after addition of TC to different concentrations of N-CQDs (insert in (c) was linear relationship of I/I_0 with concentration of TC in the range of 3.32–32.26 μM). (The number of repeat experiments was five times).

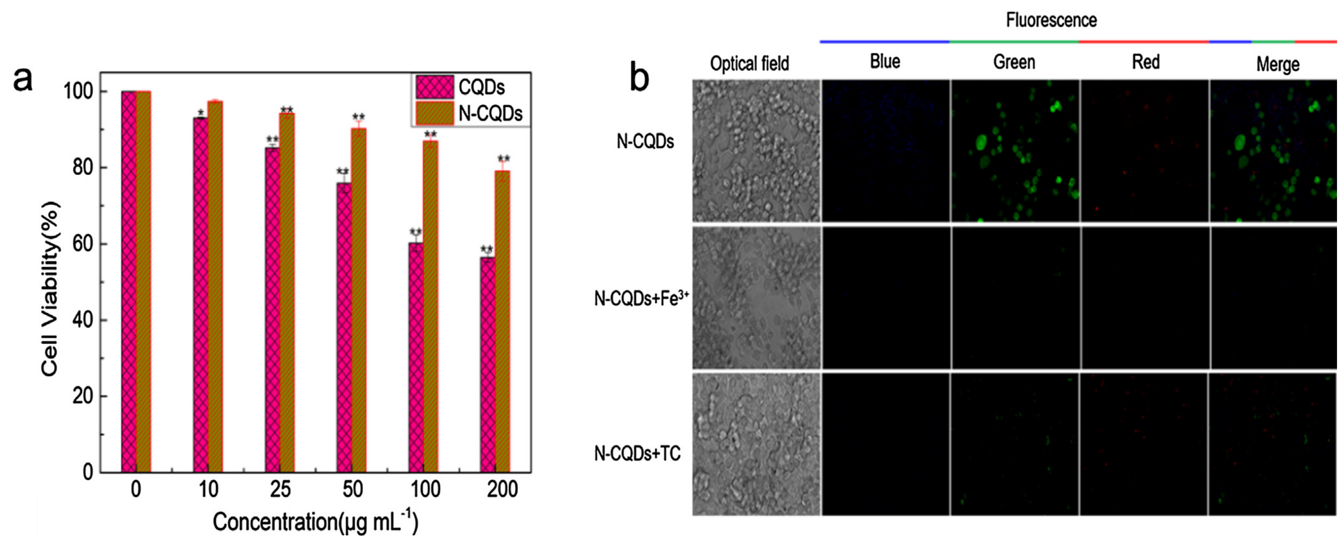

Fig. 5. (a) Cell viability of the HepG2 cells after incubation with the photoluminescent N-CQDs and CQDs for 24 h. (b) Fluorescence fluorescent microscopy images of HepG2 cells treated with 200 μg mL^{-1}N-CQDs for 2 h at three different excitation wavelengths including 435 (Blue), 525 (Green) and 597 nm (Red). (The number of repeat experiments was three times). (For interpretation of the references to colour in this figure legend, the reader is referred to the web version of this article.)

Table1
Test results of fluorescence probe method applied for TC in tap water and river water samples (n = 5).

Samples	TC (μM) Added	Found	Recoveries (%)	RSD (n = 5, %)
River water	5	4.9363 ± 0.0531	98.73 ± 1.06	1.26
	15	15.642 ± 0.0231	104.28 ± 0.15	1.22
	25	25.8553 ± 0.1205	103.42 ± 0.48	1.32
Tap water	5	4.8497 ± 0.1231	96.99 ± 2.46	0.89
	15	14.497 ± 0.5417	96.65 ± 3.61	0.95
	25	24.2384 ± 0.6872	96.95 ± 2.75	0.84

were carried out (Fig. 5a). The cell viability of the HepG2 cells after incubation with N-CQDs and CQDs for 24 h at concentrations including 0, 10, 25, 50, 100 and 200 μg mL^{-1} has been assessed. The cytotoxicity of N-CQDs was lower than that of CQDs (*$p < 0.05$, **$p < 0.01$, Student's *t*-test). The cell survival viability of N-CQDs and CQDs at 200 μg mL^{-1} was 56.47% and 79.11%, respectively. The cell viability remained greater than 85% at 100 μg mL^{-1}, indicating the low toxicity and excellent biocompatibility of the N-CQDs. Consequently, N-CQDs could be employed in cell imaging due to their low toxicity and good cellular compatibility.

Cell imaging. To demonstrate the feasibility of using N-CQDs in fluorescent cell imaging, HepG2 cells were incubated with N-CQDs at the concentration of 200 μg mL^{-1} and observed using fluorescence microscopy. At different wavelengths of 435, 525 and 597 nm, the cells emitted multicolored fluorescence such as blue, green and red, respectively (Fig. 5b). The intracellular regions of N-CQDs-treated HepG2 cells exhibited strong green fluorescence, demonstrating that the N-CQDs penetrated the cell membranes or translocate into cells by endocytosis. However, the bright N-CQDs were added in the Fe^{3+} and TC, the cells showed noticeably weaker intracellular fluorescence (Fig. 5b N-CQDs + Fe^{3+}, N-CQDs + TC). Subsequently, the surface functional groups of N-CQDs combined with $Fe^{3+}$and TC to form the complex compounds. The complex compounds could transfer charge and energy to show the fluorescence quenching behavior. Meanwhile, the cell morphology had no important change and showed good biocompatibility of N-CQDs. It thus indicates that the N-CQDs can be applied for effective imaging of Fe^{3+} and TC in live cells.

3.7. Determination of real samples

To check the application for N-CQDs in the real water samples, different concentrations of TC were added into the real sample and measured by different methods (Fluorescence spectra and UV – vis) to determine the TC concentrations. The value was based on the previously obtained regression curve. The recoveries for detecting TC in real water samples ranged from 96.65% to 104.28% (Table 1).

To confirm the accuracy of our experiment, different concentrations of TC in those water samples were measured by UV–vis. The concentrations of TC were compared for different measurement modes (Table S2). The data of TC in real water were in accordance by UV–vis and fluorescence method. The comparing values were almost similar. These values demonstrated that the fluorescence method test is feasible for quickly and accurately detecting the TC in practical applications.

4. Conclusion

In summary, N-CQDs (QY = 23.48%) were successfully synthesized using rice residue and glycine via a facile, ecofriendly and repeatable one-step hydrothermal method. XPS and FT-IR analysis supported the successful doping of nitrogen into the framework of the CQDs. The N-CQ*Ds* with an average size of 2.70 nm exhibited excellent solubility, high stability, high fluorescence intensity and excitation-dependent PL behavior. HRTEM images of N-CQDs showed that most particles were amorphous carbon without obvious lattice fringes. The broad application capability of N-CQDs has been demonstrated: (i) a fluorescent probe for Fe^{3+} with demonstrated high selectivity and sensitivity; (ii) detection of TCs such as TC, OTc and CTc. The LODs of TC, OTc, and CTc were 0.2367, 0.3739 and 0.2791 μM, respectively; (iii) because of their good stability and low biotoxicity, the multicolored N-CQDs were used in vitro in fluorescent bioimaging. The fluorescent images demonstrated that the probe was cell-permeable and could effectively detect Fe^{3+} and TC in the living cells. Eventually, compared with heavy weight of metals or ceramics [49-55] and relatively poor thermal stability of polymers and their nanocomposites [53,56-69], the N-CQDs have an appealing potential for bioimaging, pollution detection, polluted water treatment [70-83], photocatalytic degradation, energy storage/conversion (such as supercapacitors, fuel cells, solar cells etc.) [84-89], electromagnetic interference (EMI) shielding [58,90-96] and drug delivery.

Acknowledgement

This work was financially supported by the National Natural Science Foundation of China (No. 31670592); the Central University Basic Scientific Research Project of China (No. 2572017EB03); and the Research Funds for the Returned People of Heilongjiang Province (No. LC2016008).

Appendix A. Supplementary material

Supplementary data to this article can be found online at https://doi.org/10.1016/j.jcis.2018.12.047.

References

[1] M. Amjadi, T. Hallaj, H. Asadollahi, Z. Song, M. Frutos, N. Hildebrandt, Facile synthesis of carbon quantum dot/silver nanocomposite and its application for colorimetric detection of methimazole, Sensor. Actust. B-Chem. 244 (2017) 425–432.

[2] Y. Shi, Y. Pan, J. Zhong, J. Yang, J. Zheng, J. Cheng, R. Song, C. Yi, Facile synthesis of gadolinium (III) chelates functionalized carbon quantum dots for fluorescence and magnetic resonance dual-modal bioimaging, Carbon 93 (2015) 742–750.

[3] R. Atchudan, T. Edison, K.R. Aseer, S. Perumal, N. Karthik, Y.R. Lee, Highly fluorescent nitrogen-doped carbon dots derived from phyllanthus acidus utilized as a fluorescent probe for label-free selective detection of Fe^{3+} ions, live cell imaging and fluorescent ink, Biosens. Bioelectron. 99 (2018) 303–311.

[4] F. Pan, X. Xiang, Y. Li, Nitrogen coordinated single atomic metals supported on nanocarbons: a new frontier in electrocatalytic CO2 reduction, Eng. Sci. 1 (2018).

[5] J. Di, J. Xia, X. Chen, M. Ji, S. Yin, Q. Zhang, H. Li, Tunable oxygen activation induced by oxygen defects in nitrogen doped carbon quantum dots for sustainable boosting photocatalysis, Carbon 114 (2017) 601–607.

[6] Z. Wang, H. Liao, H. Wu, B. Wang, H. Zhao, M. Tan, Fluorescent carbon dots from beer for breast cancer cell imaging and drug delivery, Anal. Methods 7 (2015) 8911–8917.

[7] T. Liu, J.X. Dong, S.G. Liu, N. Li, S.M. Lin, Y.Z. Fan, J.L. Lei, H.Q. Luo, N.B. Li, Carbon quantum dots prepared with polyethyleneimine as both reducing agent and stabilizer for synthesis of Ag/CQDs composite for Hg^{2+} ions detection, J. Hazard. Mater. 322 (2017) 430–436.

[8] R. Zhang, W. Chen, Nitrogen-doped carbon quantum dots: Facile synthesis and application as a "turn-off" fluorescent probe for detection of Hg^{2+} ions, Biosens. Bioelectron. 55 (2014) 83–90.

[9] L. Li, C. Wang, J. Luo, Q. Guo, K. Liu, K. Liu, W. Zhao, Y. Lin, Fe^{3+}-functionalized carbon quantum dots: A facile preparation strategy and detection for ascorbic acid in rat brain microdialysates, Talanta 144 (2015) 1301–1307.

[10] M. Amjadi, J.L. Manzoori, T. Hallaj, N. Azizi, Sulfur and nitrogen co-doped carbon quantum dots as the chemiluminescence probe for detection of Cu^{2+} ions, J. Lumin. 182 (2017) 246–251.

[11] Y. Dong, R. Wang, G. Li, C. Chen, Y. Chi, G. Chen, Polyamine-functionalized carbon quantum dots as fluorescent probes for selective and sensitive detection of copper ions, Anal. Chem. 84 (2012) 6220–6224.

[12] P. Singhal, B.G. Vats, S.K. Jha, S. Neogy, Green, Water-dispersible photoluminescent On-Off-On probe for selective detection of fluoride ions, ACS Appl. Mater. Inter. 9 (2017) 20536–20544.

[13] D. Pooja, S. Saini, A. Thakur, B. Kumar, S. Tyagi, M.K. Nayak, A "Turn-On" thiol functionalized fluorescent carbon quantum dot based chemosensory system for arsenite detection, J. Hazard. Mater. 328 (2017) 117–126.

[14] H. Li, C. Sun, R. Vijayaraghavan, F. Zhou, X. Zhang, D.R. MacFarlane, Long lifetime photoluminescence in N, S co-doped carbon quantum dots from an ionic liquid and their applications in ultrasensitive detection of pesticides, Carbon 104 (2016) 33–39.

[15] Y. Huang, J. Zhou, H. Feng, J. Zheng, H.M. Ma, W. Liu, C. Tang, H. Ao, M. Zhao, Z. Qian, A dual-channel fluorescent chemosensor for discriminative detection of glutathione based on functionalized carbon quantum dots, Biosens. Bioelectron. 86 (2016) 748–755.

[16] B.B. Campos, R. Contreras-Cáceres, T.J. Bandosz, J. Jiménez-Jiménez, E. Rodríguez-Castellón, J.C.G. Esteves da Silva, M. Algarra, Carbon dots as fluorescent sensor for detection of explosive nitrocompounds, Carbon 106 (2016) 171–178.

[17] C. Tang, Z. Qian, Y. Qian, Y. Huang, M. Zhao, H. Ao, H. Feng, A fluorometric and real-time assay for α-glucosidase activity through supramolecular self-assembly and its application for inhibitor screening, Sensor. Actust. B-Chem. 245 (2017) 282–289.

[18] L. Wang, B. Li, F. Xu, X. Shi, D. Feng, D. Wei, Y. Li, Y. Feng, Y. Wang, D. Jia, Y. Zhou, High-yield synthesis of strong photoluminescent N-doped carbon nanodots derived from hydrosoluble chitosan for mercury ion sensing via smartphone APP, Biosens. Bioelectron. 79 (2016) 1–8.

[19] Q. Sun, S. Fang, Y. Fang, Z. Qian, H. Feng, Fluorometric detection of cholesterol based on beta-cyclodextrin functionalized carbon quantum dots via competitive host-guest recognition, Talanta 167 (2017) 513–519.

[20] N. Li, S.G. Liu, Y.Z. Fan, Y.J. Ju, N. Xiao, H.Q. Luo, N.B. Li, Adenosine-derived doped carbon dots: From an insight into effect of N/P co-doping on emission to highly sensitive picric acid sensing, Anal. Chim. Acta 1013 (2018) 63–70.

[21] Z. Li, Y. Zhang, Q. Niu, M. Mou, Y. Wu, X. Liu, Z. Yan, S. Liao, A fluorescence probe based on the nitrogen-doped carbon dots prepared from orange juice for detecting Hg^{2+} in water, J. Lumin. 187 (2017) 274–280.

[22] Y. Guo, L. Zhang, F. Cao, Y. Leng, Thermal treatment of hair for the synthesis of sustainable carbon quantum dots and the applications for sensing Hg^{2+}, Sci. Rep. 6 (2016) 35795.

[23] S. Thambiraj, D. Ravi Shankaran, Green synthesis of highly fluorescent carbon quantum dots from sugarcane bagasse pulp, Appl. Surf. Sci. 390 (2016) 435–443.

[24] C. Cheng, Y. Shi, M. Li, M. Xing, Q. Wu, Carbon quantum dots from carbonized walnut shells: Structural evolution, fluorescence characteristics, and intracellular bioimaging, Mater. Sci. Eng. C 79 (2017) 473–480.

[25] M. Wu, Y. Wang, W. Wu, C. Hu, X. Wang, J. Zheng, Z. Li, B. Jiang, J. Qiu, Preparation of functionalized water-soluble photoluminescent carbon quantum dots from petroleum coke, Carbon 78 (2014) 480–489.

[26] Z. Zhang, W. Sun, P. Wu, Highly photoluminescent carbon dots derived from egg white: Facile and green synthesis, photoluminescence properties, and multiple applications, ACS Sustain. Chem. Eng. 3 (2015) 1412–1418.

[27] J. Yu, N. Song, Y.K. Zhang, S.X. Zhong, A.J. Wang, J. Chen, Green preparation of carbon dots by Jinhua bergamot for sensitive and selective fluorescent detection of Hg^{2+} and Fe^{3+}, Sensor. Actust. B-Chem. 214 (2015) 29–35.

[28] T. Madrakian, S. Maleki, S. Gilak, A. Afkhami, Turn-off fluorescence of amino-functionalized carbon quantum dots as effective fluorescent probes for determination of isotretinoin, Sensor. Actust. B-Chem. 247 (2017) 428–435.

[29] F. Niu, Y. Xu, J. Liu, Z. Song, M. Liu, J. Liu, Controllable electrochemical/electroanalytical approach to generate nitrogen-doped carbon quantum dots from varied amino acids: pinpointing the utmost quantum yield and the versatile photoluminescent and electrochemiluminescent applications, Electrochim. Acta. 236 (2017) 239–251.

[30] X. Wang, R.Y. Li, S.Y. Fan, Z.J. Li, G.G. Wang, Z.G. Gu, J.K. Liu, D-penicillamine-functionalized graphene quantum dots for fluorescent detection of Fe^{3+} in iron supplement oral liquids, Sensor. Actust. B-Chem. 243 (2017) 211–220.

[31] S. Zhang, J. Li, M. Zeng, J. Xu, X. Wang, W. Hu, Polymer nanodots of graphitic carbon nitride as effective fluorescent probes for the detection of Fe^{3+} and Cu^{2+} ions, Nanoscale 6 (2014) 4157–4162.

[32] P. Liu, P.F. Borrell, M. Bozic, V. Kokol, K. Oksman, A.P. Mathew, Nanocelluloses and their phosphorylated derivatives for selective adsorption of Ag^{+}, Cu^{2+} and Fe^{3+} from industrial effluents, J. Hazard. Mater. 294 (2015) 177–185.

[33] P.B. Pati, S.S. Zade, MLCT based colorimetric probe for iron having D–A–D type architecture of benzo[2,1,3]thiadiazole acceptor and thiophene donor with azomethine pendant arm, Inorg. Chem. Commun. 39 (2014) 114–118.

[34] Y. Feng, D. Zhong, H. Miao, X. Yang, Carbon dots derived from rose flowers for tetracycline sensing, Talanta 140 (2015) 128–133.

[35] C. Nebot, M. Guarddon, F. Seco, A. Iglesias, J.M. Miranda, C.M. Franco, A. Cepeda, Monitoring the presence of residues of tetracyclines in baby food samples by HPLC-MS/MS, Food Control 46 (2014) 495–501.

[36] S.M. Taghdisi, N.M. Danesh, M. Ramezani, K. Abnous, A novel M-shape electrochemical aptasensor for ultrasensitive detection of tetracyclines, Biosens. Bioelectron. 85 (2016) 509–514.

[37] H. Xu, H.Y. Mi, M.M. Guan, H.Y. Shan, Q. Fei, Y.F. Huan, Z.Q. Zhang, G.D. Feng, Residue analysis of tetracyclines in milk by HPLC coupled with hollow fiber membranes-based dynamic liquid-liquid micro-extraction, Food Chem. 232 (2017) 198–202.

[38] R. Liu, J. Zhang, M. Gao, Z. Li, J. Chen, D. Wu, P. Liu, A facile microwave-hydrothermal approach towards highly photoluminescent carbon dots from goose feathers, Rsc. Adv. 5 (2015) 4428–4433.

[39] Y. Sun, H. Miao, S. Ma, L. Zhang, C. You, F. Tang, C. Yang, X. Tian, F. Wang, Y. Luo, X. Lin, H. Wang, C. Li, Z. Li, H. Yu, X. Liu, Y. Xiao, Y. Gong, J. Zhang, H. Quan, C. Xie, FePt-Cys nanoparticles induce ROS-dependent cell toxicity, and enhance

chemo-radiation sensitivity of NSCLC cells in vivo and in vitro, Cancer Lett. 418 (2018) 27–40.
[40] L. Li, C. Wang, K. Liu, Y. Wang, K. Liu, Y. Lin, Hexagonal cobalt oxyhydroxide-carbon dots hybridized surface: high sensitive fluorescence turn-on probe for monitoring of ascorbic acid in rat brain following brain ischemia, Anal. Chem. 87 (2015) 3404–3411.
[41] B. Shi, Y. Su, L. Zhang, M. Huang, R. Liu, S. Zhao, Nitrogen and phosphorus co-doped carbon nanodots as a novel fluorescent probe for highly sensitive detection of Fe^{3+} in human serum and living cells, ACS Appl. Mater. Inter. 8 (2016) 10717–10725.
[42] R. Zare-Dorabei, S.M. Ferdowsi, A. Barzin, A. Tadjarodi, Highly efficient simultaneous ultrasonic-assisted adsorption of Pb(II), Cd(II), Ni(II) and Cu (II) ions from aqueous solutions by graphene oxide modified with 2,2'-dipyridylamine: central composite design optimization, Ultrason. Sonochem. 32 (2016) 265–276.
[43] D.R. Kumar, S. Kesavan, T.T. Nguyen, J. Hwang, C. Lamiel, J.-J. Shim, Polydopamine@electrochemically reduced graphene oxide-modified electrode for electrochemical detection of free-chlorine, Sensor. Actust. B-Chem. 240 (2017) 818–828.
[44] S.J. Zhu, Q.N. Meng, L. Wang, J.H. Zhang, Y.B. Song, H. Jin, K. Zhang, H.K. Sun, et al., Highly photoluminescent parbon dots for multicolor patterning, sensors, and bioimaging, Angew. Chem. Int. Ed. 52 (2013) 3953–3957.
[45] L. Chen, C. Wu, P. Du, X. Feng, P. Wu, C. Cai, Electrolyzing synthesis of boron-doped graphene quantum dots for fluorescence determination of Fe^{3+} ions in water samples, Talanta 164 (2017) 100–109.
[46] Z. Chen, D. Lu, G. Zhang, J. Yang, C. Dong, S. Shuang, Glutathione capped silver nanoclusters-based fluorescent probe for highly sensitive detection of Fe^{3+}, Sensor. Actust. B-Chem. 202 (2014) 631–637.
[47] P. Devi, G. Kaur, A. Thakur, N. Kaur, A. Grewal, P. Kumar, Waste derivitized blue luminescent carbon quantum dots for selenite sensing in water, Talanta 170 (2017) 49–55.
[48] J. Shangguan, J. Huang, D. He, X. He, K. Wang, R. Ye, X. Yang, T. Qing, J. Tang, Highly Fe^{3+}-selective fluorescent nanoprobe based on ultrabright N/P codoped carbon dots and its application in biological samples, Anal. Chem. 89 (2017) 7477–7484.
[49] Z. Zhao, R. Guan, J. Zhang, Z. Zhao, P. Bai, Effects of process parameters of semisolid stirring on microstructure of Mg-3Sn-1Mn-3SiC (wt%) strip processed by rheo-rolling, Acta Metall. Sin. (Engl. Lett.) 30 (2017) 66–72.
[50] Z. Zhao, P. Bai1, R. Guan, V. Murugadoss, H. Liu, X. Wang, Z. Guo, Microstructural evolution and mechanical strengthening mechanism of Mg-3Sn-1Mn-1La alloy after heat treatments, Mater. Sci. Eng. A 734 (2018) 200–209.
[51] Y. Zhao, L. Qi, Y. Jin, K. Wang, J. Tian, P. Han, The structural, elastic, electronic properties and Debye temperature of $D0_{22}$-Ni_3V under pressure from first-principles, J. Alloys Compounds 647 (2015) 1104–1110.
[52] Y. Zhao, S. Deng, H. Liu, J. Zhang, Z. Guo, H. Hou, First-principle investigation of pressure and temperature influence on structural, mechanical and thermodynamic properties of Ti_3AC_2 (A=Al and Si), Comput. Mater. Sci. 154 (2018) 365–370.
[53] Z. Wang, H. Zhu, N. Cao, R. Du, Y. Liu, G. Zhao, Superhydrophobic surfaces with excellent abrasion resistance based on benzoxazine/mesoporous SiO_2, Mater. Lett. 186 (2017) 274–278.
[54] W. Deng, T. Kang, H. Liu, J. Zhang, N. Wang, N. Lu, Y. Ma, A. Umar, Z. Guo, Potassium hydroxide activated and nitrogen doped graphene with enhanced supercapacitive behavior, Sci. Adv. Mater. 10 (2018) 937–949.
[55] B. Kirubasankar, V. Murugadoss, J. Lin, T. Ding, M. Dong, H. Liu, J. Zhang, T. Li, N. Wang, Z. Guo, S. Angaiaha, In-situ grown nickel selenide onto graphene nanohybrid electrodes for high energy density asymmetric supercapacitors, Nanoscale 10 (2018) 20414–20425.
[56] C. Wang, Z. He, X. Xie, X. Mai, Y. Li, T. Li, M. Zhao, C. Yan, H. Liu, E. Wujcik, Z. Guo, Controllable cross-linking anion exchange membranes with excellent mechanical and thermal properties, Macromol. Mater. Eng. 3 (2018) 1700462.
[57] C. Wang, B. Mo, Z. He, Q. Shao, D. Pan, E. Wujick, J. Guo, X. Xie, X. Xie, Z. Guo, Crosslinked norbornene copolymer anion exchange membrane for fuel cells, J. Membrane Sci. 556 (2018) 118–125.
[58] L. Wang, H. Qiu, C. Liang, P. Song, Y. Han, Y. Han, J. Gu, J. Kong, D. Pan, Z. Guo, Electromagnetic Interference Shielding MWCNT-Fe_3O_4@Ag/Epoxy Nanocomposites with Satisfactory Thermal Conductivity and High Thermal Stability, Carbon 141 (2019) 506–514.
[59] J. Gu, Y. Li, C. Liang, Y. Tang, L. Tang, Y. Zhang, J. Kong, H. Liu, Z. Guo, Synchronously improved dielectric and mechanical properties of wave-transparent laminated composites combining with outstanding thermal stability by incorporating iysozyme/POSS functionalized PBO fibers, J. Mater. Chem. C 6 (2018) 7652–7660.
[60] Z. Hu, Q. Shao, Y. Huang, L. Yu, D. Zhang, X. Xu, J. Lin, H. Liu, Z. Guo, Light triggered interfacial damage self-healing of poly(p- phenylene benzobisoxazole) fiber composites, Nanotechnology 29 (2018) 185602.
[61] C. Wang, B. Mo, Z. He, C.X. Zhao, L. Zhang, Q. Shao, X. Guo, E. Wujcik, Z. Guo, Hydroxide ions transportation in polynorbornene anion exchange membrane, Polymer 138 (2018) 363–368.
[62] M. Dong, Q. Li, H. Liu, C. Liu, E. Wujcik, Q. Shao, T. Ding, X. Mai, C. Shen, Z. Guo, Thermoplastic polyurethane-carbon black nanocomposite coating: fabrication and solid particle erosion resistance, Polymer 158 (2018) 381–390.
[63] H. Gu, H. Zhang, C. Ma, X. Xu, Y. Wang, Z. Wang, R. Wei, H. Liu, C. Liu, Q. Shao, X. Mai, Z. Guo, Trace electrosprayed nanopolystyrene facilitated dispersion of multiwalled carbon nanotubes: simultaneously strengthening and toughening epoxy, Carbon 142 (2019) 131–140.
[64] Y. Li, T. Jing, G. Xu, J. Tian, M. Dong, Q. Shao, B. Wang, Z. Wang, Y. Zheng, C. Yang, Z. Guo, 3-D magnetic graphene oxide-magnetite poly(vinyl alcohol) nanocomposite substrates for immobilizing enzyme, Polymer 149 (2018) 13–22.
[65] X. Cui, G. Zhu, Y. Pan, Q. Shao, C. Zhao, M. Dong, Y. Zhang, Z. Guo, Polydimethylsiloxane-titania nanocomposite coating: fabrication and corrosion resistance, Polymer 138 (2018) 203–210.
[66] Y. He, S. Yang, H. Liu, et al., Reinforced carbon fiber laminates with oriented carbon nanotube epoxy nanocomposites: magnetic field assisted alignment and cryogenic temperature mechanical properties, J. Colloid Interf. Sci. 517 (2018) 40–51.
[67] Y. Zhang, M. Zhao, J. Zhang, Q. Shao, J. Li, H. Li, B. Lin, M. Yu, S. Chen, Z. Guo, Excellent corrosion protection performance of epoxy composite coatings filled with silane functionalized silicon nitride, J. Polymer Research 25 (2018) 130.
[68] Y. Kong, Y. Li, G. Hu, J. Lin, D. Pan, D. Dong, E. Wujick, Q. Shao, M. Wu, J. Zhao, Z. Guo, Preparation of polystyrene-b-poly(ethylene/propylene)-b-polystyrene grafted glycidyl methacrylate and its compatibility with recycled polypropylene/recycled high impact polystyrene blends, Polymer 145 (2018) 232–241.
[69] Z. Hu, D. Zhang, F. Lu, W. Yuan, X. Xu, Q. Zhang, H. Liu, Q. Shao, Z. Guo, Y. Huang, Multistimuli-responsive intrinsic self-healing epoxy resin constructed by host−guest interactions, Macromolecules 51 (2018) 5294–5303.
[70] Y. Ma, L. Lyu, Y. Guo, Y. Fu, Q. Shao, T. Wu, S. Guo, K. Sun, X. Guo, E.K. Wujcik, Z. Guo, Porous lignin based poly (acrylic acid)/organo-montmorillonite nanocomposites: swelling behaviors and rapid removal of Pb (II) ions, Polymer 128 (2017) 12–23.
[71] Y. Wang, P. Zhou, S. Luo, S. Guo, J. Lin, Q. Shao, X. Guo, Z. Liu, J. Shen, B. Wang, Z. Guo, In situ polymerized PAA/alumina nanocomposites for Pb^{2+} adsorption, Adv. Poly. Technol. (2018), https://doi.org/10.1002/adv.21969.
[72] Y. Wang, P. Zhou, S. Luo, X. Liao, B. Wang, Q. Shao, X. Guo, Z. Guo, Controllable synthesis of monolayer poly(acrylic acid) on channel surface of mesoporous alumina for Pb(II) adsorption, Langmuir 34 (2018) 7859–7868.
[73] K. Gong, Q. Hu, L. Yao, M. Li, D. Sun, Q. Shao, B. Qiu, Z. Guo, Ultrasonic pretreated sludge derived stable magnetic active carbon for Cr(VI) removal from wastewater, ACS Sustain. Chem. Eng. 6 (2018) 7283–7291.
[74] J. Huang, Y. Cao, Q. Shao, X. Peng, Z. Guo, Magnetic nanocarbon adsorbents with enhanced hexavalent chromium removal: morphology dependence of fibrillar vs particulate structures, Ind. Eng. Chem. Res. 56 (2017) 10689–10701.
[75] X. Zhang, X. Wang, X. Liu, J. Lv, Y. Wang, G. Zheng, H. Liu, C. Liu, Z. Guo, C. Shen, Porous polyethylene bundles with enhanced hydrophobicity and pumping oil-recovery ability via skin-peeling, ACS Sustain. Chem. Eng. 6 (2018) 12580–12585.
[76] Z. Li, B. Wang, X. Qin, Y. Wang, C. Liu, Q. Shao, N. Wang, J. Zhang, Z. Wang, C. Shen, Z. Guo, Superhydrophobic/superoleophilic polycarbonate/carbon nanotubes porous monolith for selective oil adsorption from water, ACS Sustain. Chem. Eng. 6 (2018) 13747–13755.
[77] Y. Qian, Y. Yuan, H. Wang, H. Liu, J. Zhang, S. Shi, Z. Guo, N. Wang, Highly efficient uranium adsorption by salicylaldoxime/polydopamine graphene oxide nanocomposites, J. Mater. Chem. A (2018), https://doi.org/10.1039/C8TA09486A. in press.
[78] H. Zhang, S. Lyu, X. Zhou, H. Gu, C. Ma, C. Wang, T. Ding, Q. Shao, H. Liu, Z. Guo, Super light 3D hierarchical nanocellulose aerogel foam with superior oil adsorption, J. Colloid Interf. Sci. 536 (2019) 245–251.
[79] K. Gong, Q. Hu, Y. Xiao, X. Cheng, H. Liu, N. Wang, B. Qiu, Z. Guo, Triple layered core-shell ZVI@carbon@polyaniline composites enhanced electron utilization in Cr(VI) reduction, J. Mater. Chem. A 6 (2018) 11119–11128.
[80] J. Huang, Y. Li, Y. Cao, F. Peng, Y. Cao, Q. Shao, H. Liu, Z. Guo, Hexavalent chromium removal over magnetic carbon nanoadsorbent: synergistic effect of fluorine and nitrogen co-doping, J. Mater. Chem. A 6 (2018) 13062–13074.
[81] K. Gong, S. Guo, Y. Zhao, Q. Hu, H. Liu, D. Sun, M. Li, B. Qiu, Z. Guo, Bacteria cell templated porous polyaniline facilitated detoxification and recovery of hexavalent chromium, J. Mater. Chem. A 6 (2018) 16824–16832.
[82] P. Zhang, T. Ge, H. Yang, S. Lin, Y. Cao, C. Zhao, H. Liu, A. Umar, Z. Guo, Antifouling of titania nanostructures in real maritime conditions, Sci. Adv. Mater. 10 (2018) 1216–1223.
[83] Z. Zhao, H. An, J. Lin, M. Feng, V. Murugadoss, T. Ding, H. Liu, Q. Shao, X. Man, N. Wang, H. Gu, S. Angaiah, Z. Guo, Progress on the photocatalytic reduction removal of chromium contamination, Chem. Rec. (2019), https://doi.org/10.1002/tcr.201800153.
[84] T. Su, Q. Shao, Z. Qin, Z. Guo, Z. Wu, Role of interfaces in two-dimensional photocatalyst for water splitting, ACS Catalysis 8 (2018) 2253–2276.
[85] W. Du, X. Wang, J. Zhan, X. Sun, L. Kang, F. Jiang, X. Zhang, Q. Shao, M. Dong, H. Liu, V. Murugadoss, Z. Guo, Biological cell template synthesis of nitrogen-doped porous hollow carbon spheres/MnO_2 composites for high-performance asymmetric supercapacitors, Electrochim. Acta 296 (2019) 907–915.
[86] M. Idrees, S. Batool, J. Kong, Q. Zhuang, H. Liu, Q. Shao, N. Lu, Y. Feng, E.K. Wujcik, Q. Gao, T. Ding, R. Wei, Z. Guo, Polyborosilazane derived ceramics - nitrogen sulfur dual doped graphene nanocomposite anode for enhanced lithium ion batteries, Electrochim. Acta 296 (2019) 925–937.
[87] H. Du, C. Zhao, J. Lin, Z. Hu, Q. Shao, J. Guo, B. Wang, D. Pan, E.K. Wujcik, Z. Guo, Carbon nanomaterials in direct liquid fuel cells, Chem. Rec. 18 (2018) 1365–1372.
[88] Y. Zhang, L. Qian, W. Zhao, X. Li, X. Huang, X. Mai, Z. Wang, Q. Shao, X. Yan, Z. Guo, Highly efficient Fe-N-C nanoparticles modified porous graphene composites for oxygen reduction reaction, J. Electrochem. Soc. 165 (2018) H510–H516.

[89] X. Lou, C. Lin, Q. Luo, J. Zhao, B. Wang, J. Li, Q. Shao, X. Guo, N. Wang, Z. Guo, Crystal-structure modification enhanced FeNb11O29 anodes for lithium-ion batteries, ChemElectroChem 4 (2017) 3171–3180.

[90] D. Jiang, V. Murugadoss, Y. Wang, J. Lin, T. Ding, Z. Wang, Q. Shao, C. Wang, H. Liu, N. Lu, R. Wei, S. Angaiah, Z. Guo, Electromagnetic interference shielding polymers and nanocomposites – a review, Polym. Rev. (2017), https://doi.org/10.1080/15583724.2018.1546737.

[91] N. Wu, C. Liu, D. Xu, J. Liu, W. Liu, Q. Shao, Z. Guo, Enhanced electromagnetic wave absorption of three-dimensional porous Fe_3O_4/C composite flowers, ACS Sustain. Chem. Eng. 6 (2018) 12471–12480.

[92] Z. Wang, R. Wei, J. Gu, H. Liu, C. Liu, C. Luo, J. Kong, Q. Shao, N. Wang, Z. Guo, X. Liu, Ultralight, highly compressible and fire-retardant graphene aerogel with self-adjustable electromagnetic wave absorption, Carbon 139 (2018) 1126–1135.

[93] C. Cheng et al., Tunable and weakly negative permittivity in carbon/silicon nitride composites with different carbonizing temperatures, Carbon 125 (2017) 103–112.

[94] C. Wang, V. Murugadoss, J. Kong, Z. He, X. Mai, Q. Shao, Y. Chen, L. Guo, C. Liu, S. Angaiah, Z. Guo, Overview of carbon nanostructures and nanocomposites for electromagnetic wave shielding, Carbon 140 (2018) 696–733.

[95] P. Xie, B. He, F. Dang, J. Lin, R. Fan, C. Hou, H. Liu, J. Zhang, Y. Ma, Z. Guo, Bio-gel derived nickel/carbon nanocomposites with enhanced microwave absorption, J. Mater. Chem. C 6 (2018) 8812–8822.

[96] P. Xie, Z. Wang, Z. Zhang, R. Fan, C. Cheng, H. Liu, Y. Liu, T. Li, C. Yan, N. Wang, Z. Guo, Silica microspheres templated self-assembly of three-dimensional carbon network with stable radio-frequency negative permittivity and low dielectric loss, J. Mater. Chem. C 6 (2018) 5239–5249.